ISSN 0036-0236, Russian Journal of Inorganic Chemistry, 2018, Vol. 63, No. 11, pp. 1484–1493. © Pleiades Publishing, Ltd., 2018.
Original Russian Text © E.P. Simonenko, N.P. Simonenko, A.N. Gordeev, A.F. Kolesnikov, E.K. Papynov, O.O. Shichalin, K.Yu. Tal'skikh, E.A. Gridasova, V.A. Avramenko, V.G. Sevastyanov, N.T. Kuznetsov, 2018, published in Zhurnal Neorganicheskoi Khimii, 2018, Vol. 63, No. 11, pp. 1465–1475.

PHYSICAL METHODS OF INVESTIGATION

Impact of a Supersonic Dissociated Air Flow on the Surface of HfB_2–30 vol % SiC UHTC Produced by the Sol–Gel Method[1]

E. P. Simonenko[a, *], N. P. Simonenko[a], A. N. Gordeev[b], A. F. Kolesnikov[b], E. K. Papynov[c, d], O. O. Shichalin[c, d], K. Yu. Tal'skikh[c, d], E. A. Gridasova[c, d], V. A. Avramenko[c, d], V. G. Sevastyanov[a], and N. T. Kuznetsov[a]

[a] *Kurnakov Institute of General and Inorganic Chemistry, Russian Academy of Sciences, Moscow, 119991 Russia*
[b] *Ishlinskii Institute of Problems of Mechanics, Russian Academy of Sciences, Moscow, 119526 Russia*
[c] *Institute of Chemistry, Far-Eastern Branch, Russian Academy of Sciences, Vladivostok, 690022 Russia*
[d] *Far-Eastern Federal University, Vladivostok, 690091 Russia*
**e-mail: ep_simonenko@mail.ru*

Received March 15, 2018

Abstract—A new method to produce ultra-high-temperature ceramic composites under rather mild conditions (1700°C, 30 MPa, treatment time 15 min) was applied to synthesize a relatively dense (ρ_{rel} = 84.5%) HfB_2–30 vol % SiC material containing nanocrystalline silicon carbide (average crystallite size ~37 nm). The elemental and phase compositions, microstructure, and some mechanical properties of this material and also its thermal behavior in an air flow within the temperature range 20–1400°C were investigated. Using a high-frequency induction plasmatron, a study was made of the effect of a supersonic dissociated air flow on the surface of the produced ultra-high-temperature ceramic composite shaped as a flat-end cylindrical sample installed into a copper water-cooled holder. On 40-min exposure of the sample to the supersonic dissociated air flow, the sample did not fail, and the weight loss was 0.04%. Although the heat flux was high, the temperature on the surface did not exceed 1400–1590°C, which could be due to the heat transfer from the sample to the water-cooled model. The thickness of the oxidized layer under these conditions was 10–20 μm; no SiC-depleted region formed. Specific features of the microstructure of the oxidized surface layer of the sample were noted.

Keywords: sol–gel technology, nanomaterial, UHTC, thermochemical impact, high-enthalpy air flow, induction plasmatron

DOI: 10.1134/S0036023618110177

INTRODUCTION

Investigations of the development of efficient methods to produce ultra-high-temperature ceramics (UHTC) based on zirconium or hafnium diboride and silicon carbide are of great scientific and practical interest [1–7]. This is due to the unique ability of such materials to withstand, without catastrophic failure, high-speed (including super- and hypersonic) air flows, which cause an increase in the temperature on the surface of parts with sharp edges to >2000°C [1, 8–15]. However, along with a set of such advantageous properties as high melting points of components and their phase stability over a wide temperature range [16–18], as well as high thermal conductivity, oxidation resistance, and hardness, there are disadvantages typical of ceramics, first of all, low crack resistance. Therefore, many recent studies have focused on improving mechanical characteristics by introducing strengthening additives (C and SiC fibers [6, 19–21], carbon nanotubes [22–24], graphene [25–27], graphite and carbon black [28–30], finely divided powders of carbides with very high melting points [7, 31–34]) or using nanodispersed components in producing UHTC [35–40].

The potential of nanostructured $ZrB_2(HfB_2)$–SiC ceramic materials prompted us to develop a new method to produce them [41, 42], by which nanocrystalline silicon carbide can be synthesized in situ by hot pressing or spark plasma sintering of MB_2–(SiO_2–C) (M = Zr, Hf) composite powder obtained by the sol–gel method. Combined DSC/TGA in an air flow within the temperature range 20–1400°C determined [41] that the oxidation resistance of samples obtained by the new method exceeds that of samples of a similar composition that were produced by spark plasma sintering from coarse crystalline powders HfB_2 and SiC with particle sizes >2 and >100 μm, respectively.

[1] Supplementary materials are available for this article at http://doi.org/10.1134/S0036023618110177 and are accessible for authorized users.

We have recently shown that [43], on long-term exposure to a subsonic high-enthalpy air flow, HfB_2–30 vol % SiC material obtained at 1700°C is oxidized to no higher extent than the previously studied samples of a similar composition [44, 45].

The purpose of this work was to study the behavior of HfB_2–30 vol % SiC ultra-high-temperature ceramic composite, which was obtained by hot pressing of finely divided HfB_2–(SiO_2–C) composite powder, on exposure to the supersonic dissociated air flow using a high-frequency induction plasmatron.

EXPERIMENTAL

HfB_2–30 vol % SiC ultra-high-temperature ceramic materials were produced using an HP20-3560-20 hot press (Thermal Technology LLC) [41]. HfB_2–(SiO_2–C) composite powder obtained by the sol–gel technology was loaded in a graphite die and compacted. The chamber was evacuated and then filled with argon, after which the pressure was brought to a desired value (30 MPa) and heating was begun at a rate of 10 deg/min to a temperature of 1700°C. The time of treatment at the maximum temperature was 15 min. As a release agent for the die, a small amount of boron nitride was used.

X-ray powder diffraction analysis was made with a Bruker D8 ADVANCE X-ray powder diffractometer (CuK_α radiation, resolution 0.02°).

The IR reflection spectra of the samples were recorded with an InfraLYuM FT-08 FTIR spectrometer using an EasiDiff diffuse reflectance accessory (PIKE Technologies) within the wavenumber range 350–4000 cm^{-1} (signal accumulation time 60 s).

Scanning electron microscopy was performed with a Carl Zeiss NVision 40 focused ion beam scanning electron microscope; the elemental composition of microregions was determined with an Oxford Instruments energy-dispersive X-ray analyzer.

The thermal behavior of products in an air flow (100 mL/min) within the temperature range 20–1400°C (heating rate 20 deg/min) was studied with an SDT Q600 TGA/DSC analyzer.

The compressive and flexural strengths of the obtained ceramic samples were determined using an AG-100kNXplus floor-type universal testing machine. The microhardness of the produced ceramics was investigated with a DUH-211S dynamic ultra micro hardness tester.

The experimental investigation of the impact of a supersonic jet of dissociated air on the sample surface was performed using a VGU-4 100-kV high-frequency induction plasmatron [2, 8, 43–45] at the Ishlinskii Institute of Problems of Mechanics, Russian Academy of Sciences, Moscow, Russia, at an anode feed power N of the plasmatron of 20 to 70 kW using a sonic nozzle with an exit diameter of 30 mm. The air flow rate was 3.6 g/s, and the pressure in the chamber was 16–20 hPa (in supersonic regime, such a pressure change does not influence the heat flux and stagnation pressure). The temperature of the surface of the sample was measured with a Mikron M-770S pyrometer in the spectral ratio pyrometer mode (temperature range 1000–3000°C, measurement spot size ~5 mm). The temperature distribution on the surface of the sample was recorded with a Tandem VS415U thermal imager. In the measurements, the wavelength was 0.9 μm, and the spectral emissivity ε was set to be 0.7 at the beginning of the experiment and was reduced to 0.6 at the 16th minute. The ε values were chosen in comparative experiments for simultaneously determining the surface temperatures of similar samples with the Tandem VS415U thermal imager and the Mikron M-770S spectral ratio pyrometer so that the readings of both instruments coincided.

The stagnation pressure P_{st} was measured with a Pitot tube with a hemispherical nose of $R = 15$ mm and an inlet diameter of 14 mm.

RESULTS AND DISCUSSION

Production and Investigation of HfB_2–30 vol % SiC Ceramic Sample

A HfB_2–SiC ultra-high-temperature ceramic composite sample containing 30 vol % SiC was obtained by hot pressing of HfB_2–(SiO_2–C) composite powder, in which the SiO_2–C system was synthesized by the sol–gel method. Specific features of the method made it possible to synthesize a finely divided system on the surface of boride particles. Components of this system were maximally uniformly distributed in each other, which favored higher reactivity. Therefore, carbothermic reduction of carbon dioxide occured at not too high temperature (1700°C) during hot pressing.

Figure 1 presents the shrinkage curve characterizing the process of forming the material and the simultaneous reaction between silicon dioxide and carbon. One can see that, after stabilization of the process parameters, the treatment of the sample resulted in quite significant shrinkage, which was due both to carbothermic synthesis and to consolidation of the ceramic sample.

The density of the obtained material was 7.4 g/cm^3 (84.5% of the value calculated by the additive method, in which the densities of HfB_2 and SiC were assumed to be 11.2 [46] and 3.2 [47] g/cm^3, respectively).

The X-ray powder diffraction analysis showed (Fig. 2) that, under the chosen heat-treatment conditions, the hot pressing of HfB_2–(SiO_2–C) composite powder was capable of producing ultra-high-temperature ceramic materials containing nanocrystalline silicon carbide. The average size of crystallites of the synthesized SiC as estimated by the Scherrer formula was 37 ± 2 nm.

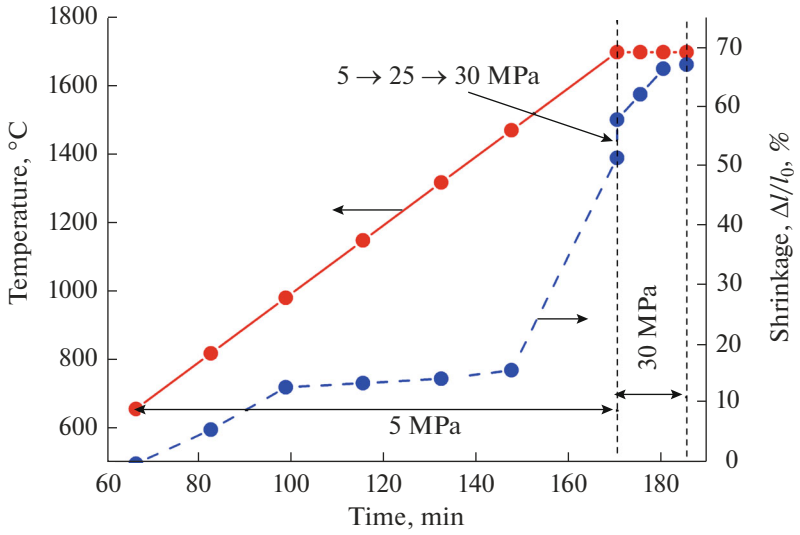

Fig. 1. Kinetic curves of shrinkage of the HfB_2–30 vol % SiC sample during hot pressing of HfB_2–(SiO_2–C) composite powder at various temperatures and pressures.

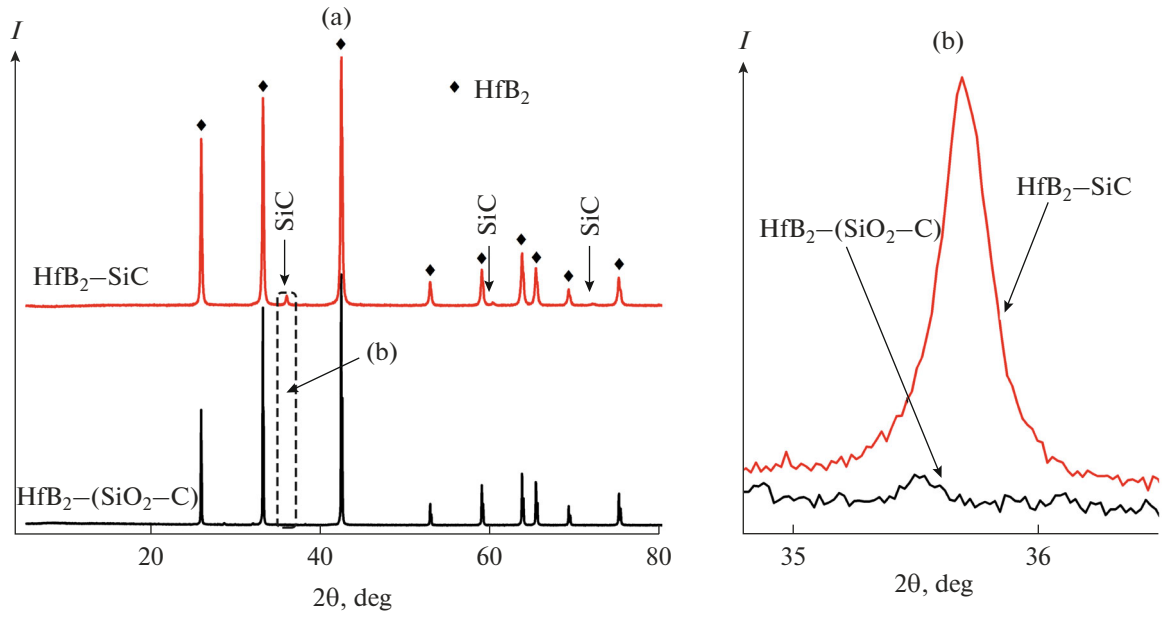

Fig. 2. (a) X-ray powder diffraction patterns of HfB_2–(SiO_2–C) powder and the HfB_2–30 vol % SiC sample and (b) portions of the patterns within the 2θ range 35°–37°.

The IR diffuse reflectance spectroscopy confirmed that silicon dioxide was completely conversed to carbide: in the spectra within the wavenumber range 970–1200 cm^{-1}, there was no broadened intense absorption band of the stretching vibrations of Si–O bonds, which is characteristic of the initial HfB_2–(SiO_2–C) powders, but there was an absorption band within the range 800–950 cm^{-1}, which corresponds to ν(Si–C).

The scanning electron microscopy of the polished sample surface of the produced composite showed that the distribution of the components HfB_2 and SiC is quite uniform; the HfB_2 grain size was ~2 μm. This value corresponds to the particle size of the initial HfB_2 powder, in which aggregates of particles were 20–30 μm in diameter; i.e., the chosen procedure for obtaining samples [41] enables one to break up these aggregates.

The investigation of the thermal behavior of the produced sample in an air flow (Fig. 3) demonstrated that the oxidation of the material, which was accompanied by weight gain, began at a temperature

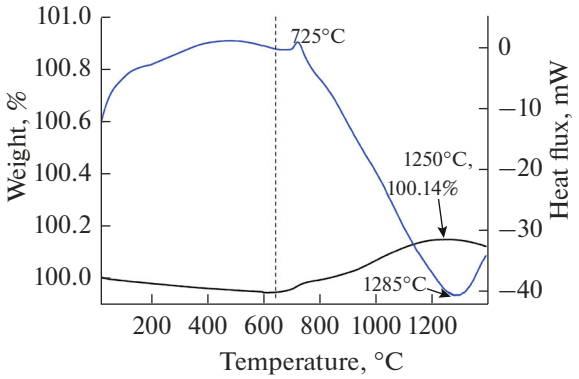

Fig. 3. DSC curve (blue line) and TGA curve (black line) for the HfB_2–30 vol % SiC sample in the air flow.

>650°C. An exothermic event with a maximum at 725°C was observed early in the weight gain, which was likely to be due to the oxidation of surface layers of the sample. Further oxidation occurred at much lower rate, which was caused by significant complication of the mechanism, including the oxygen diffusion through the borosilicate glass layer formed at temperatures >850–900°C. The weight gain to 1250°C was 0.14%, and the further tendency of the weight to insignificantly decrease can be attributed to processes of high-temperature evaporation of glass components, first of all, boron oxide.

The compressive and flexural strengths of the obtained composite with a porosity of 15.5% were 284 and 199 MPa, respectively. The microhardness of HV0.5 material was 14.5 ± 1.9 GPa (10 s).

Investigation of the Behavior of HfB_2–30 vol % SiC Ultra-High-Temperature Ceramic Material on Exposure to a Supersonic Dissociated Air Flow

To study the behavior of the produced HfB_2–30 vol % SiC ceramic composite materials on heating on exposure to a supersonic dissociated air flow using the VGU-4 induction plasmatron, a sample were installed into an assembled copper model comprising a mandrel (into which a sample was pushed) and a water-cooled holder (into which the mandrel was inserted with a sliding fit). The thermal contact on the end face was guaranteed by the spring action of a tension pin; the contact surfaces were greased with a thermal paste, which significantly improved the heat transfer from the mandrel to the water-cooled holder.

The sample was flush-mounted in the model using three SiC whisker wool filaments, which reduced the heat transfer from the sample to the model. A conical sonic nozzle with an exit diameter of 30 mm was used, the distance from which to the sample was 25 mm.

The sample was introduced to a dissociated air jet at an anode feed power of the plasmatron of 20 kW and a pressure of 16 ± 1 hPa. Then, the anode feed power

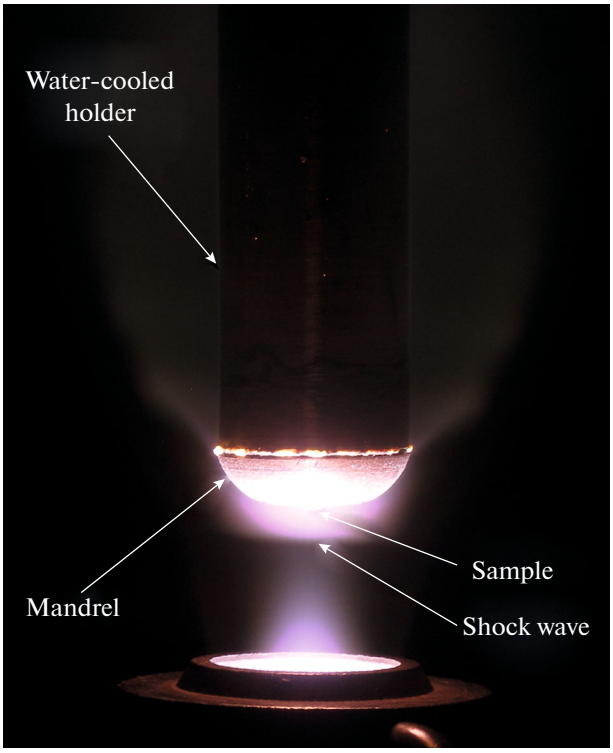

Fig. 4. Supersonic dissociated air flow (N = 60 kW, P_{st} = 65.8 hPa, q = 691 W/cm^2) past the model with the installed HfB_2–30 vol % SiC sample.

was increased stepwise to 70 kW at a step of 10 kW; in this process, the heat flux toward the highly catalytic copper surface increased from 232 to 779 W/cm^2. The duration of the exposure at the first five steps was 5 min, and the total exposure time was 40 min. Figure 4 presents the photograph of the supersonic high-enthalpy air flow past the model with the sample.

The measurement of the average surface temperature with the spectral ratio pyrometer showed (Fig. 5; Table 1) that, with stepwise increasing anode feed power of the plasmatron, the surface temperature of the sample correspondingly increased. At the early steps (at N = 20 and 30 kW), the average temperature tended to decrease with time at constant flow parameters, and beginning with N = 50 kW (q = 598 W/cm^2), the average temperature increased by 35–40 deg in 5 min. This could be related to the fact that an oxidation product with higher catalytic activity than borosilicate glass emerged on the surface: this is HfO_2, which also reduced the surface emissivity. This was likely to be due to the intense evaporation of components of borosilicate glass at relatively low pressure (18 hPa). The high catalytic activity of the surface at the late steps of exposure was also indicated by a noticeable (by 35 deg) increase in temperature with a short-time increase of the pressure in the chamber from 16.6 to 20.6 hPa (despite a certain simultaneous decrease in the anode feed power).

The thermal imager data demonstrated (Fig. 6) that, after the introduction of the sample to the dissociated air jet, the temperature distribution over the surface of the sample was quite uniform (Suppl. 1). With increasing anode feed power of the plasmatron, the temperature also increased. Somewhat (by approximately 80–100 deg) underestimated temperature data can be explained by the fact that the emissivity values used in the recording were too high in comparison with the actual values.

Unlike the experiments with the subsonic air jet, in which the temperature was maximum at the edges of the sample [2, 8, 43–45], on exposure to the supersonic high-enthalpy flow, the temperature was maximum in the central part of the sample (Fig. 7). The maximum temperature difference over the surface was ~80–90 deg.

Thus, despite the high values of the heat flux acting on the sample, the surface temperature did not exceed 1590°C, which can be explained by the high heat transfer from the sample to the copper water-cooled model. For 40 min of the experiment, no formation of overheated regions was observed. The weight loss was 0.04%.

Figure 8b presents the appearance of the sample after exposure to the supersonic dissociated air flow. It is seen that, in spite of the long exposure, no white porous ceramic layer formed on the surface. The surface of the sample is light-gray, with the central part of the sample being the lightest, probably, due to the maximum oxidation.

The X-ray powder diffraction analysis showed that the phase composition of the oxidized layer somewhat differs depending on the temperature reached on the surface of the sample (Fig. 9). The dominant phase is monoclinic HfO_2. Moreover, the hafnon $HfSiO_4$ phase is also present, the content of which in the central part of the sample is 7%, and at the periphery, in regions in which the temperature was 80–90 deg lower than that at the center, the hafnon content is to a certain extent (~11%) higher.

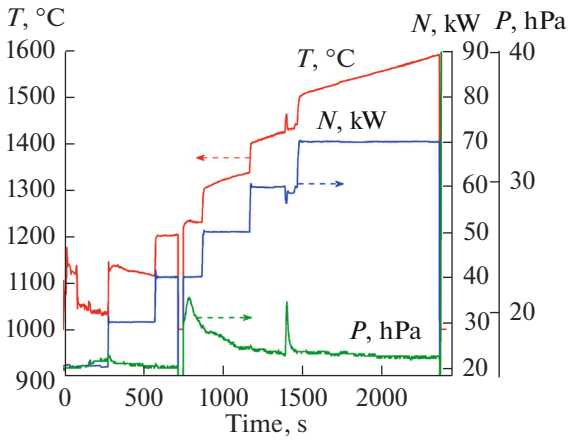

Fig. 5. Average surface temperature (according to the pyrometer data) of the HfB_2–SiC sample at various anode powers N of the plasmatron, pressures P in the chamber, and exposure durations.

The microstructure of the surface of the sample after exposure to the high-enthalpy air flow was studied by scanning electron microscopy. It was determined that the microstructure of central (relatively "hot") regions (Fig. 10) differs to some extent from that of regions at the edge of the sample, where the temperature was lower (Fig. 11).

Furthermore, it differs significantly from the microstructure formed on exposure of samples of a similar chemical composition to the subsonic dissociated air flow [2, 8, 43–45]. It was previously shown that, after the temperature on the surface under thermochemical action reached 1500–1700°C, a smooth borosilicate glass layer formed, under which a porous HfO_2 framework lay. However, the exposure of the sample to the supersonic flow in the most heated

Table 1. Average surface temperature T_{pyr} of the sample (as measured with a spectral ratio pyrometer) at various exposure times and process parameters: anode power N of the plasmatron, pressure P in the chamber of the plasmatron, heat flux q, and stagnation pressure P_{st}

Time, min	N, kW	P, hPa	q, W/cm^2	P_{st}, hPa	T_{pyr}, °C
0–5	20	16	232	50.2	1170 → 1030
5–10	30	16	363	55.8	1140 → 1120
10–15*	40	16 → 21 → 19	484	59.6	1200 → 1235
15–20	50	18 → 17	598	62.5	1300 → 1340
20–25	60	17	691	65.8	1400 → 1440
25–30	70	17 → 16	779	68.7	1505 → 1540
35	70	16	779	68.7	1570
40	70	16	779	68.7	1590

* At the 13th minute at an anode feed power of 40 kW, the discharge was turned off, and in 40 min, the sample was reintroduced to the jet at the same power but at a pressure of 21 hPa. The time of treatment at N = 40 kW was increased to 5 min, which was characteristic of the other steps.

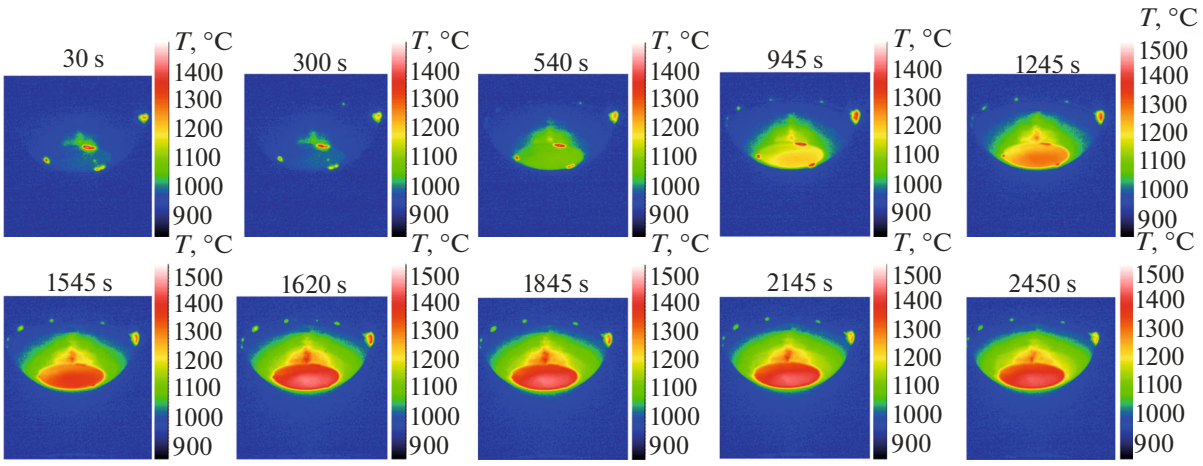

Fig. 6. Thermal images of the surface of the HfB_2–30 vol % SiC sample at various times of exposure to the supersonic dissociated air flow. Three overheated points around the sample (top) formed by the burnout of residues of SiC whiskers used for holding the sample in the holder.

region (at the center, the maximum temperature ≤1600°C, Fig. 10) gave rise to an inverse distribution of the layers: the micrographs show that, in deeper layers between finely divided, often fibrous, HfO_2 particles, there is a glass layer, in which, in highest-temperature regions, pore formed from bubbles of evaporating borosilicate glass.

In regions where the temperatures were still lower (at the periphery of the sample, the maximum temperature 1400°C, Fig. 11), the scanning electron microscopy images show that the borosilicate glass formed early in the oxidation, albeit close to the surface, is partially covered by compact aggregates of particles based on hafnium dioxide 200–300 nm in diameter.

The energy-dispersive X-ray elemental analysis of both regions demonstrated that the atomic ratio n(Hf) : n(Si) both in the central part and in the periphery of the sample is ~1.2–1.3, which confirmed the presence of a protective borosilicate glass layer near the surface.

The optical microscopy study of the microstructure of the polished surface of the sample showed (Fig. 12) that the thicknesses of the oxidized layers in regions where the temperatures reached on exposure to the supersonic dissociated air flow were different are virtually the same. The scanning electron microscopy confirmed this conclusion. Fixation of the sample in epoxy resin led to the separation of the oxidized layer from the rest of the sample: the micrograph demonstrates a crack (Fig. 13). This can result from a significant difference in thermal expansion coefficient between the oxidation products and HfB_2–SiC composite.

As Fig. 13 shows, the average thickness of the oxidized layer was 10–20 μm; the mapping of the silicon and hafnium distributions over the polished surface of the sample failed to detect a region depleted in silicon carbide, which was present on exposure of the sample of a similar composition to the subsonic dissociated air

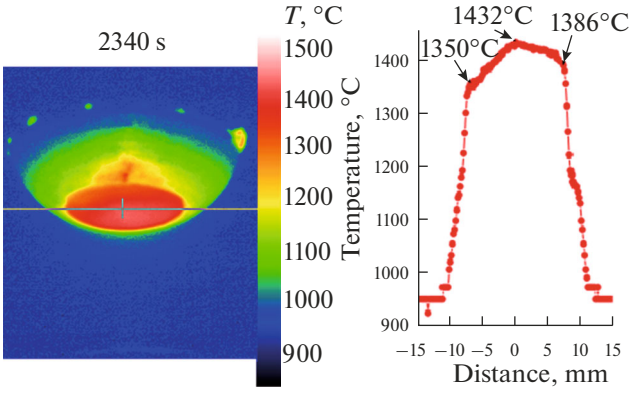

Fig. 7. (a) Thermal image of the surface of the HfB_2–30 vol % SiC sample at the 39th minute of exposure and (b) the corresponding temperature distributions across the indicated line.

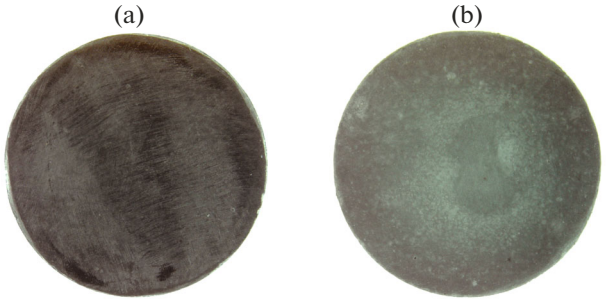

Fig. 8. Appearance of the exposed surface of the HfB_2–30 vol % SiC sample (a) before and (b) after exposure to the supersonic dissociated air flow.

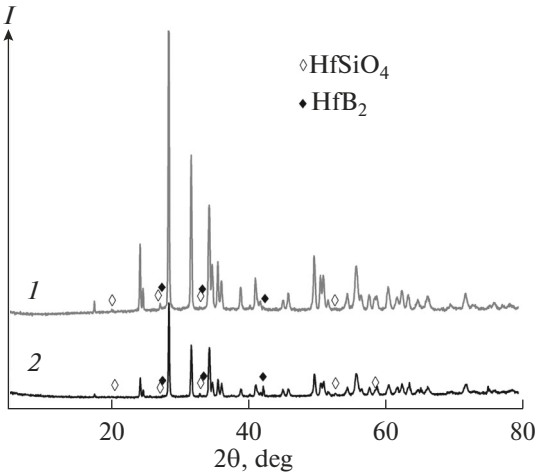

Fig. 9. X-ray powder diffraction patterns of the oxidized surface of the HfB_2–30 vol % SiC sample at the (*1*) central and (*2*) peripheral parts after exposure to the supersonic dissociated air flow. Reflections of the (empty diamonds) tetragonal $HfSiO_4$ and (filled diamonds) hexagonal HfB_2 phases are indicated; the other reflections correspond to the monoclinic HfO_2 phase.

flow [43]. The energy-dispersive X-ray analysis showed that, in microregion 1 in the oxidized layer, the hafnium oxide content is elevated: n(Hf) : n(Si) = 3.1, whereas at points 2–4 at different distances from the surface, this ratio is the same and is 0.4, which coincides with the calculated value of the n(Hf) : n(Si) ratio for the HfB_2–30 vol % SiC composition.

CONCLUSIONS

Thus, we showed that the new method to produce UHTC by compacting HfB_2–(SiO_2–C) composite powder, which was synthesized by the sol–gel technology, by hot pressing under rather mild conditions (1700°C, 30 MPa, treatment time 15 min) ensures, simultaneously with the carbothermic synthesis of SiC, the formation of a relatively dense (ρ_{rel} = 84.5%) material containing nanocrystalline silicon carbide (average crystallite size ~37 nm). At a porosity of the sample of 15.5%, the microhardness of the material was 14.5 ± 1.9 GPa, the compressive strength was 284 MPa, and the and flexural strength was 199 MPa.

Using the high-frequency induction plasmatron, the study was made of the effect of the supersonic dissociated air flow on the surface of the produced HfB_2–30 vol % SiC ultra-high-temperature ceramic composite shaped as the flat-end cylindrical sample installed into the copper water-cooled holder.

It was determined that, on 40-min exposure of the sample to the supersonic dissociated air flow (N = 20–70 kW, P_{ch} = 16–21 hPa, q = 232–779 W/cm^2, P_{st} = 50.2–68.7 hPa), the sample did not fail, and the weight loss was 0.04%. In spite of the high heat flux,

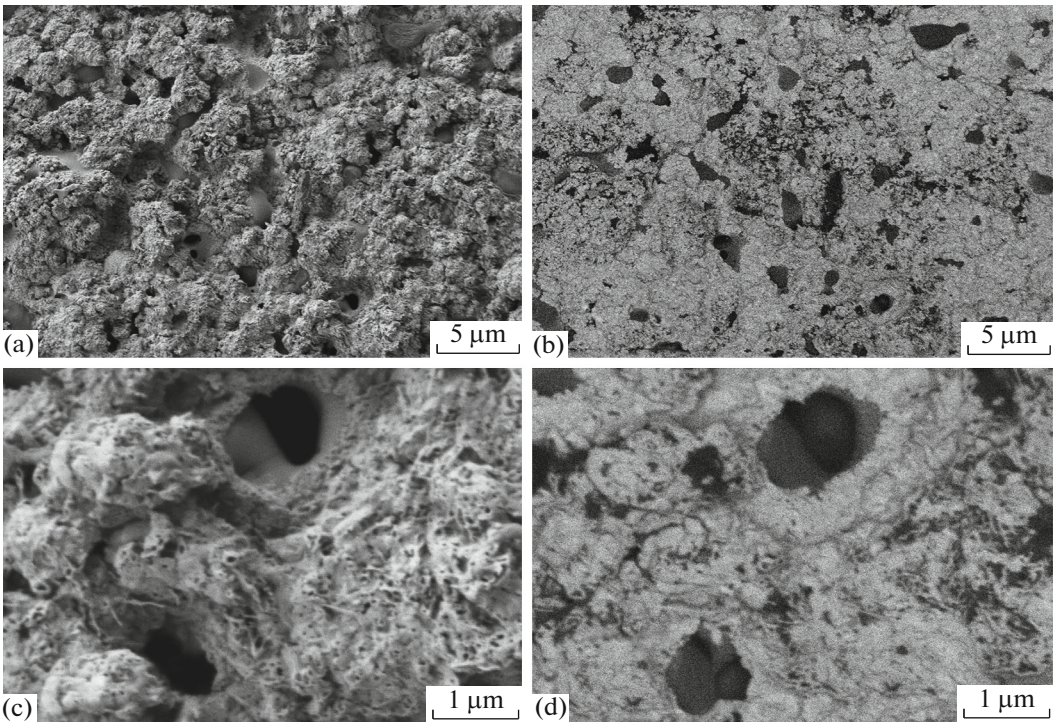

Fig. 10. Microstructure of the central, relatively hot, region of the surface of the sample after exposure to the supersonic dissociated air flow (maximum temperature 1600°C): (a, c) in mode of detection of secondary electrons and (b, d) in atomic number contrast mode.

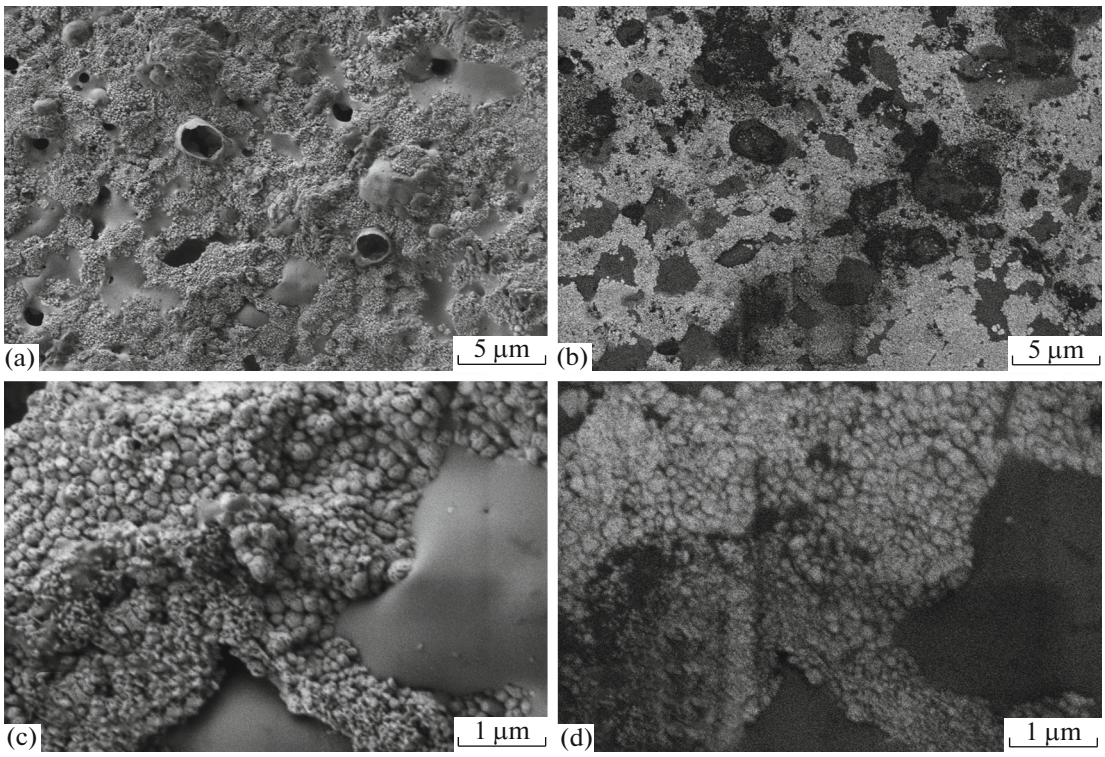

Fig. 11. Microstructure of the relatively cold region of the surface of the sample after exposure to the supersonic dissociated air flow (maximum temperature 1400°C): (a, c) in mode of detection of secondary electrons and (b, d) in atomic number contrast mode.

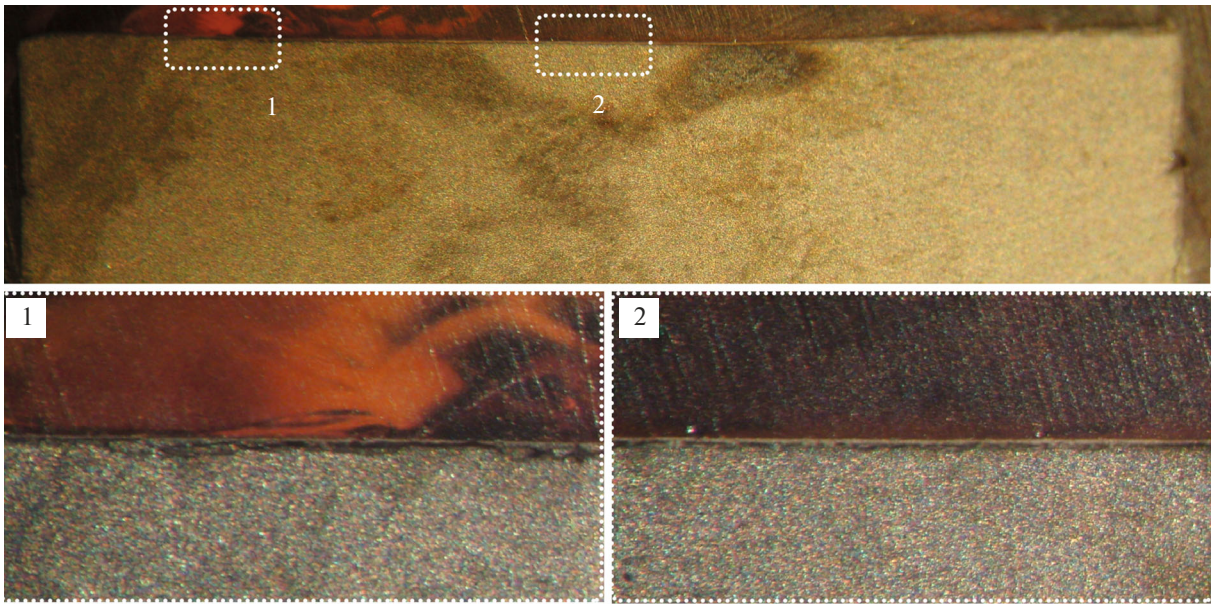

Fig. 12. Microstructure of the polished surface of the HfB_2–30 vol % SiC sample after exposure to the supersonic dissociated air flow according to the optical microscopy data in (1) low- and (2) high-temperature regions.

the temperature on the surface did not exceed 1400–1590°C. This suggested that, despite precautions to prevent the contact between the sample and the copper water-cooled holder (mounting and insulation using SiC whisker wool filaments), much of the heat was transferred to the model. The thickness of the oxidized layer under these conditions was 10–20 μm; no SiC-depleted region formed.

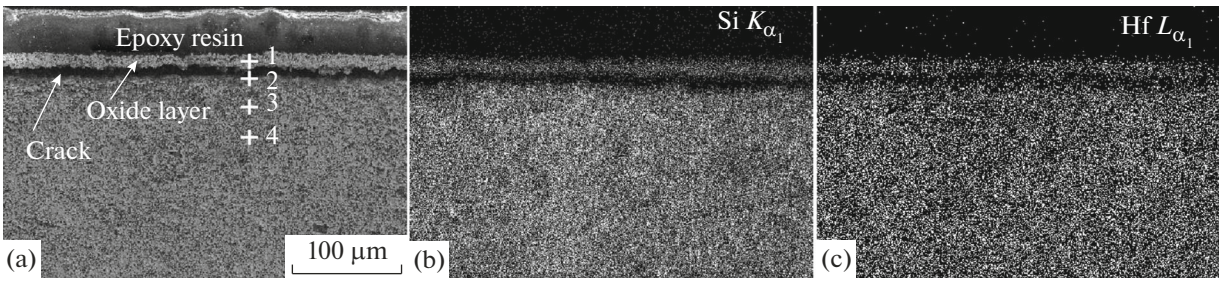

Fig. 13. Microstructure of the polished surface of the HfB_2–30 vol % SiC sample after exposure to the supersonic dissociated air flow (the sample is fixed in epoxy resin) according to the scanning electron microscopy data and the Si and Hf elemental distributions.

The microstructure of the oxidized surface layer of the sample differed from that of the samples subjected to the subsonic dissociated air flow [3, 8, 43–45]. For example, although the temperatures were not too high (<1600°C), no borosilicate glass concentrated on the surface; in the most heated region (at the center), on the surface, finely divided fibrous HfO_2-dominated particles formed, between which, in deeper layers, a glass layer could be seen. At the periphery of the sample, where the surface temperature was ~1400°C, borosilicate glass was closer to the surface, but was partially covered by compact aggregates of particles based on hafnium dioxide 200–300 nm in diameter, which probably formed by the evaporation of the volatile components SiO_2 and B_2O_3. Such a microstructure can be due to the relatively low values of the pressure in the chamber of the plasmatron and, hence, of the oxygen content, which favors vapor formation.

ACKNOWLEDGMENTS

This work was supported by the Russian Science Foundation (project no. 17-73-20181).

REFERENCES

1. E. P. Simonenko, D. V. Sevast'yanov, N. P. Simonenko, et al., Russ. J. Inorg. Chem. **58**, 1669 (2013). doi 10.1134/S0036023613140039
2. E. P. Simonenko, A. N. Gordeev, N. P. Simonenko, et al., Russ. J. Inorg. Chem. **61**, 1203 (2016). doi 10.1134/S003602361610017X
3. R. Savino, L. Criscuolo, G. D. Di Martino, et al., J. Eur. Ceram. Soc. (2018) (in press). doi 10.1016/j.jeurceramsoc.2017.12.043
4. L. Silvestroni, H.-J. Kleebe, W. G. Fahrenholtz, and J. Watts, Sci. Rep. **7**, Art. no. 40730 (2017). doi 10.1038/srep40730
5. K. S. Cissel and E. Opila, J. Am. Ceram. Soc. **101**, 1765 (2018). doi 10.1111/jace.15298
6. M. Shahedi Asl, Ceram. Int. **43**, 15047 (2017). doi 10.1016/j.ceramint.2017.08.030
7. J. Zou, V. Rubio, and J. Binner, Acta Mater. **133**, 293 (2017). doi 10.1016/j.actamat.2017.05.033
8. E. P. Simonenko, N. P. Simonenko, A. N. Gordeev, et al., Russ. J. Inorg. Chem. **63**, 421 (2018). doi 10.1134/S0036023618040186
9. F. Monteverde, A. Cecere, and R. Savino, J. Eur. Ceram. Soc. **37**, 2325 (2017). doi 10.1016/j.jeurceramsoc.2017.01.018
10. T. A. Parthasarathy, M. D. Petry, M. K. Cinibulk, et al., J. Am. Ceram. Soc. **96**, 907 (2013). doi 10.1111/jace.12180
11. A. Cecere, R. Savino, C. Allouis, and F. Monteverde, Int. J. Heat Mass Transfer **91**, 747 (2015). doi 10.1016/j.ijheatmasstransfer.2015.08.029
12. X. Jin, R. He, X. Zhang, and P. Hu, J Alloys Compd. **566**, 125 (2013). doi 10.1016/j.jallcom.2013.03.067
13. F. Monteverde and R. Savino, J. Am. Ceram. Soc. **95**, 2282 (2012). doi 10.1111/j.1551-2916.2012.05226.x
14. X. Zhang, P. Hu, J. Han, and S. Meng, Compos. Sci. Technol. **68**, 1718 (2008). doi 10.1016/j.compscitech.2008.02.009
15. F. Monteverde, R. Savino, M. De Stefano Fumo, and A. Di Maso, J. Eur. Ceram. Soc. **30**, 2313 (2010). doi 10.1016/j.jeurceramsoc.2010.01.029
16. R. W. Olesinski and G. J. Abaschian, Bull. Alloy Phase Diagrams **5**, 486 (1984).
17. H. Bittermann and P. Rogl, J. Phase Equilib. **18**, 24 (1997).
18. H. Duschanek and P. Rogl, *Phase Diagrams of Ternary Metal–Boron–Carbon Systems*, Ed. by G. Effenberg (ASM International, Materials Park, OH, Stuttgart, 1998), p. 445.
19. A. Vinci, L. Zoli, E. Landi, and D. Sciti, Corros. Sci. **123**, 129 (2017). doi 10.1016/j.corsci.2017.04.012
20. D. Sciti, R. Savino, and L. Silvestroni, J. Eur. Ceram. Soc. **32**, 1837 (2012). doi 10.1016/j.jeurceramsoc.2012.01.019
21. K. Gui, P. Hu, W. Hong, et al., J. Alloys Compd. **706**, 16 (2017). doi 10.1016/j.jallcom.2017.02.227
22. A. Nisar and K. Balani, Coatings **7**, 110/1 (2017). doi 10.3390/coatings7080110
23. A. Nisar, S. Ariharan, and K. Balani, Ceram. Int. **43**, 13483 (2017). doi 10.1016/j.ceramint.2017.07.053
24. A. Nisar, S. Ariharan, T. Venkateswaran, et al., Carbon **111**, 269 (2017). doi 10.1016/j.carbon.2016.10.002
25. X. Zhang, Y. An, J. Han, et al., RSC Adv. **5**, 47060 (2015). doi 10.1039/C5RA05922D

26. B. Zhang, X. Zhang, C. Hong, et al., ACS Appl. Mater. Interfaces **8**, 11675 (2016). doi 10.1021/acsami.6b00822
27. M. Shahedi Asl and M. Ghassemi Kakroudi, Mater. Sci. Eng., A **625**, 385 (2015). doi 10.1016/j.msea.2014.12.028
28. X. Chen, X. Peng, Z. Wei, et al., Mater. Des. **126**, 91 (2017). doi 10.1016/j.matdes.2017.04.001
29. I. Farahbakhsh, Z. Ahmadi, and M. Shahedi Asl, Ceram. Int. **43**, 8411 (2017). doi 10.1016/j.ceramint.2017.03.188
30. L. Wang, D. Kong, G. Fang, and J. Liang, Int. J. Appl. Ceram. Technol. **14**, 31 (2017). doi 10.1111/ijac.12613
31. S. Guo, J. Mater. Sci. **53**, 4010 (2018). doi 10.1007/s10853-017-1850-7
32. Z. Balak, M. Azizieh, H. Kafashan, et al., Mater. Chem. Phys. **196**, 333 (2017). doi 10.1016/j.matchemphys.2017.04.062
33. H.-B. Ma, J. Zou, J.-T. Zhu, et al., Acta Mater. **129**, 159 (2017). doi 10.1016/j.actamat.2017.02.052
34. Y. Kubota, M. Yano, R. Inoue, et al., J. Eur. Ceram. Soc. **38**, 1095 (2018). doi 10.1016/j.jeurceramsoc.2017.11.024
35. W. Hong, K. Gui, P. Hu, et al., J. Adv. Ceram. **6**, 110 (2017). doi 10.1007/s40145-017-0223-7
36. P. Hu, K. Gui, W. Hong, and X. Zhang, Mater. Lett. **200**, 14 (2017). doi 10.1016/j.matlet.2017.04.089
37. P. Hu, K. Gui, W. Hong, et al., J. Eur. Ceram. Soc. **37**, 2317 (2017). doi 10.1016/j.jeurceramsoc.2017.02.008
38. M. Mashhadi, H. Khaksari, and S. Safi, J. Mater. Res. Technol. **4**, 416 (2015). doi 10.1016/j.jmrt.2015.02.004
39. W. Han, S. Zhou, and J. Zhang, Ceram. Int. **40**, 16665 (2014). doi 10.1016/j.ceramint.2014.08.028
40. Z. Zhong, L. Yan, L. Liu, and B. Xu, Ceram. Int. **43**, 3462 (2017). doi 10.1016/j.ceramint.2016.11.171
41. E. P. Simonenko, N. P. Simonenko, E. K. Papynov, et al., Russ. J. Inorg. Chem. **63**, 1 (2018). doi 10.1134/S0036023618010187
42. N. T. Kuznetsov, V. G. Sevastyanov, E. P. Simonenko, and N. P. Simonenko, RU Patent No. 2618567 (May 4, 2017).
43. E. P. Simonenko, N. P. Simonenko, A. N. Gordeev, et al., Russ. J. Inorg. Chem. **63**, 1345 (2018). doi 10.1134/S0036023618100170
44. V. G. Sevastyanov, E. P. Simonenko, A. N. Gordeev, et al., Russ. J. Inorg. Chem. **58**, 1269 (2013). doi 10.1134/S003602361311017X
45. V. G. Sevastyanov, E. P. Simonenko, A. N. Gordeev, et al., Russ. J. Inorg. Chem. **59**, 1361 (2014). doi 10.1134/S0036023614120250
46. W. Wong-Ng and C. Hubbard, Powder Diffr. **2**, 242 (1987). doi 10.1017/S0885715600012884
47. T. Kawamura, Mineral. J. **4**, 333 (1965). doi 10.2465/minerj1953.4.333

Translated by V. Glyanchenko